Absence of the Spindle Assembly Checkpoint restores mitotic fidelity upon loss of sister chromatid cohesion

Running title: SAC inhibition rescues cohesion-related mitotic defects

Rui D. Silva[1,*], Mihailo Mirkovic[2,*], Leonardo G. Guilgur[2], Om S. Rathore[1], Rui Gonçalo Martinho[1,3,#] and Raquel A. Oliveira[2, #]

1- Departamento de Ciências Biomédicas e Medicina, and Center for Biomedical Research, Universidade do Algarve, Campus de Gambelas, Faro, Portugal.

2- Instituto Gulbenkian de Ciência. Oeiras, Portugal.

3- Instituto de Medicina Molecular, Faculdade de Medicina, Universidade de Lisboa, Lisboa, Portugal.

* These authors contributed equally to the work

Correspondence should be addressed to RAO rcoliveira@igc.gulbenkian.pt or RGM rgmartinho@ualg.pt

ORCID id: Rui Gonçalo Martinho (orcid.org/0000-0002-1641-3403)
ORCID id: Raquel A. Oliveira (orcid.org/0000-0002-8293-8603)

Abstract

Sister chromatid cohesion is essential for faithful mitosis, as premature cohesion loss leads to random chromosome segregation and aneuploidy, resulting in abnormal development. To identify specific conditions capable of restoring defects associated with cohesion loss, we screened for genes whose depletion modulates *Drosophila* wing development when sister chromatid cohesion is impaired. Cohesion deficiency was induced by knock-down of the acetyltransferase Separation anxiety (San)/Naa50, a cohesin complex stabilizer. Several genes whose function impacts wing development upon cohesion loss were identified. Surprisingly, knockdown of key Spindle Assembly Checkpoint (SAC) proteins, Mad2 and Mps1, suppressed developmental defects associated with San depletion. SAC impairment upon cohesin removal, triggered by San depletion or artificial removal of the cohesin complex, prevented extensive genome shuffling, reduced segregation defects and restored cell survival. This counterintuitive phenotypic suppression was caused by an intrinsic bias for efficient chromosome bi-orientation at mitotic entry, coupled with slow engagement of error-correction reactions. We conclude that mitotic timing determines the severity of defects associated with cohesion deficiency. Therefore, although divisions are still error-prone, SAC inactivation enhances cell survival and tissue homeostasis upon cohesion loss.

46 **Introduction**

47

48 Mitosis is a dynamic culmination of the cell cycle, consisting of rapid packaging,
49 alignment and partitioning of the replicated chromosomes. This process has to be
50 tightly regulated and synchronous, as defective segregation leads to aneuploidy, a
51 key hallmark of cancer and other human pathological conditions. The fidelity of
52 mitosis depends on cohesive forces that keep sister chromatids together. Sister
53 chromatid cohesion is mediated by cohesin, a tripartite ring complex that
54 embraces sister chromatid fibers from the time of their replication until the
55 subsequent mitosis (Guacci et al., 1997; Haering et al., 2008; Michaelis et al., 1997).
56 Cleavage of cohesin by separase, a cysteine protease, marks the anaphase onset,
57 where single chromatids are dragged to the poles by the mitotic spindle after
58 cohesive forces are destroyed (Uhlmann et al., 1999; Uhlmann et al., 2000).
59 Cohesin's association with chromatin is regulated by numerous factors that ensure
60 its loading, stability and dual mode of chromatin release (reviewed in (Mirkovic
61 and Oliveira, 2017)). Among those, the N-terminal acetyltransferase Separation
62 anxiety (San) (also known as Naa50) is required for establishment and/or
63 maintenance of sister chromatid cohesion, and was recently proposed to acetylate
64 the N-terminus of Rad21 cohesin subunit and regulate the interaction between
65 Rad21 and Smc3 (Hou et al., 2007; Ribeiro et al., 2016; Rong et al., 2016; Williams
66 et al., 2003). Accordingly, defects associated with San knock-down can be
67 efficiently suppressed by several conditions that enhance cohesin stability on
68 chromatin (Ribeiro et al., 2016).

69

70 Loss of sister chromatid cohesion is catastrophic for the cell as premature release
71 of cohesive forces leads to random chromosome segregation. Genome
72 randomization is highly enhanced upon cohesin loss as the presence of isolated
73 sisters chromatids triggers continuous engagement of the error–correction
74 machinery, resulting in extensive shuffling of chromatids between cell poles
75 (Mirkovic et al., 2015; Oliveira et al., 2010). Error correction mechanisms are
76 mediated by the Aurora-B kinase, which is able to sense the degree of tension
77 across and/or between kinetochores and release erroneous chromosomal
78 attachments that are not under tension (Foley and Kapoor, 2013; Khodjakov and

79 Pines, 2010; Nezi and Musacchio, 2009). Upon cohesin loss, isolated chromatids
80 lack the opposing forces to ensure proper tension and consequently undergo
81 cycles of chromosome attachment and de-attachment, in a futile attempt to achieve
82 chromosome biorientation. Consequently, mitosis in absence of cohesion results in
83 random chromosome segregation, with close to absolute probability of generating
84 aneuploid cells.
85
86 Premature release of cohesive forces during mitosis is prevented by a safeguard
87 mechanism known as the Spindle Assembly Checkpoint (SAC) (reviewed in (Foley
88 and Kapoor, 2013; Musacchio and Salmon, 2007). In the presence of unattached
89 kinetochores, this safeguard mechanism prolongs mitosis by inhibiting the
90 Anaphase Promoting Complex/Cyclosome (APC/C). SAC ensures that cohesin
91 cleavage does not occur until all chromosomes are bioriented by blocking the
92 APC/C, whose activation is needed for separase activity. In contrast to its known
93 role as a safeguard mechanism for mitotic fidelity, we describe the unexpected
94 observation that removal of the SAC alleviates mitotic errors when sister
95 chromatid cohesion is compromised.
96

97 ## Results

98

99 ***Drosophila* wing modifier screen reveals that depletion of Mad2 and Mps1**
100 **suppresses the developmental defects associated with loss of cohesion.**
101 Although the consequences of cohesin loss in unicellular organisms and cultured
102 cells are well established, its impact on tissue proliferation and morphogenesis is
103 poorly understood. To probe for conditions that would enhance or suppress
104 cellular and tissue responses to cohesion defects, we performed a modifier screen
105 in the adult *Drosophila* wing. We focused our analysis on the regulatory N-terminal
106 acetyltransferase San, as our previous work demonstrated that knock-down of this
107 protein during development gives rise to an intermediate adult wing phenotype
108 that is sensitive to phenotypic modulation (Figure 1A,B) (Ribeiro et al., 2016). To
109 search for modifiers (enhancers and suppressors) of the adult wing phenotype
110 induced by San depletion, we co-expressed the *san* RNAi with 2955 RNAis, which
111 theoretically depletes 2920 gene products, specifically in larvae imaginal wing
112 discs (using the Nubbin-Gal4 driver (Brand and Perrimon, 1993; Ng et al., 1996;
113 Wu and Cohen, 2002) (Figure 1A). The resulting wings were scored in 5 categories,
114 according to the severity of the phenotype (Figure 1C) (Ribeiro et al., 2016). Co-
115 expression of *san* RNAi and a control RNAi transgene did not modify the adult wing
116 phenotype when compared to *san* RNAi transgene alone (Figure 1E) (Ribeiro et al.,
117 2016). Any isolated enhancer gene whose depletion alone resulted in adult wings
118 phenotypes was discarded (Fig. S1). All tested RNAi lines and scored wing
119 phenotypes are shown in Tables S1 to S4.

120

121 We identified 19 suppressors and 10 enhancers whose depletion specifically
122 modified the *san* RNAi adult wing phenotype (Table 1) (Figure S1). As expected,
123 the screen revealed components previously implicated in cohesin dynamics (*Mau2*
124 and *eco*), validating its accuracy at isolating modifiers of cohesion state (Table 1)
125 (Ribeiro et al., 2016). This approach also identified the cohesion component
126 *vtd*/RAD21 RNAi as a modifier of *san* RNAi adult wing phenotype (Ribeiro et al.,
127 2016). Most of the 29 genes identified in the screen, were already characterized in
128 *Drosophila* and/or in other species (Table 2). About half of the identified genes
129 were either related with mitosis (*Claspin*, *asp*, *Mps1*, *Eb1*, *eco*, *Mau2*, *γTub23C* and

130 *mad2*) or with gene expression (CG5589, *JMJD7*, *Pabp2*, *His3* and *jumu*). Other
131 identified genes were described to be important for maintaining apicobasal cell
132 polarity and for actin cytoskeleton organization (*capu*, *cno* and *Cad99C*). We
133 identified additional suppressors/enhancer genes related with different metabolic
134 processes (*Sfxn1-3*, CG3842, *Dhap-at*, and *MFS18*), protein glycosylation
135 (CG11388), synaptic adhesion (*Nlg4*), a paralogue of Naa20 N-terminal
136 acetyltransferase (CG31730), and DNA repair/transcription (*Parp*). Surprisingly,
137 two of the strongest suppressors were proteins that participate in the SAC, Mps1
138 and Mad2, and whose depletion specifically suppressed *san* RNAi adult wing
139 phenotypes (Figure 1D,E). Given that both of these proteins belong to the same
140 biological pathway, and both were isolated as suppressors of *san* RNAi, we
141 hypothesized that impairment of SAC could rescue mitotic defects caused by
142 cohesin deficiency.
143
144 **SAC inactivation rescues chromosome segregation defects associated with**
145 **loss of cohesion.**
146 To gain further insight on whether SAC inactivation could indeed rescue cohesion
147 defects we sought out to evaluate mitotic fidelity in various experimental
148 conditions. Live cell imaging analysis in the developing wing disc revealed, as
149 expected by our previous work (Ribeiro et al., 2016), that upon *san* RNAi, cells
150 exhibited various degrees of sister chromatid cohesion defects. In control strains
151 all cells underwent mitosis with normal metaphase morphology (Figure 2A, Figure
152 S2 and Movie S1). Upon san RNAi only 13±10% displayed normal mitosis and most
153 cells underwent partial or full sister chromatid separation (17±6 and 70±13%,
154 respectively), resulting in SAC activation and extended mitosis (Figure 2A,B, Figure
155 S2 and Movie S2). More severe defects were obtained when cohesion loss was
156 induced by acute artificial cleavage of cohesin Rad21 subunit, using a previously
157 established TEV protease-mediated cleavage method (Pauli et al., 2008). In these
158 experiments, wing imaginal discs were allowed to develop normally until 3rd instar
159 larvae stage, when TEV protease was induced by heat-shock. After heat-shock
160 Rad21 became quickly undetectable in cells expressing exclusively TEV-sensitive
161 Rad21-EGFP (Figure S3). TEV expression resulted in full sister chromatid

162 separation across all cells analysed (Figure S2), leading to extended mitosis and
163 chromatid shuffling between the poles (Figure 2C,D and movie S3).
164
165 In order to inhibit the SAC, we focused on genetic conditions that remove Mad2, a
166 key component of this checkpoint, as to date this protein is thought to be solely
167 required for SAC response (in contrast to Mps1 that has been implicated in other
168 mitotic functions (Liu and Winey, 2012). Flies carrying null alleles for the *mad2*
169 gene were previously shown to be viable (Buffin et al., 2007) and its depletion in
170 the larvae wing imaginal disc did not compromise wing development (Figure 1E).
171 As expected, removal of Mad2 by RNAi or the *mad2*^{P} null allele abolished the
172 mitotic delay in both experimental conditions for cohesion loss, *san* RNAi and TEV-
173 mediated Rad21 cleavage (Figure 2A,B,C,D and Movies S4 and S5). More
174 importantly, shortening of mitotic timing drastically reduced the frequency of
175 abnormal anaphase figures (Figure 2E,F). Whereas upon premature loss of cohesin
176 mitotic exit often displays lagging chromatids or chromatin bridges, these
177 segregation defects were significantly reduced when SAC was removed (Figure 2
178 E,F).
179
180 The aforementioned analysis of mitotic defects does not account for numerical
181 errors in chromosome segregation. Therefore, a parallel evaluation of
182 chromosome distribution symmetry was performed in early syncytial blastoderm
183 embryos, as segregation efficiency of the synchronously dividing nuclei can be
184 more accurately evaluated. Cohesin cleavage in *Drosophila* syncytial embryos was
185 induced by microinjection of TEV protease during interphase, as previously
186 described (Oliveira et al., 2010). This led to full separation of sister chromatids
187 after NEBD and a short mitotic delay (Figure 3A,B, movies S6, S7). To test if such
188 mitotic delay was SAC dependent, we performed similar experiments in a *mad2*
189 mutant background. Mitotic duration under these conditions was indistinguishable
190 from controls, implying that SAC surveillance is responsible for the delay in mitotic
191 progression upon premature loss of sister chromatid cohesion (Figure 3A,B,
192 movies S8). To evaluate chromosome distribution we measured the area occupied
193 by centromeres in the vicinity of each pole as well as those lagging behind the
194 segregation plane, ending up in the middle of the segregation plane during mitotic

195 exit (most likely due to merotelic attachments) (Figure 3C). Segregation symmetry
196 was evaluated as a ratio between the areas occupied by each cluster of
197 centromeres (Cid-EGFP) during mitotic exit. As expected, this value was close to
198 one in control strains (Figure 3D). TEV-mediated cohesin cleavage caused a high
199 degree of asymmetry between centromeric signals placed at the poles (Figure 3D).
200 Moreover, TEV-cleavage resulted in the presence of lagging chromosomes during
201 anaphase (Figure 3E). Consistent with our previous results (Figure 2), loss of SAC
202 led to a significant reduction of the segregation error frequency after TEV-cleavage,
203 as evidenced by the significant recovery in centromere distribution symmetry and
204 the decrease in lagging centromeres (Figure 3D,E).
205 Altogether, these results demonstrate that SAC inactivation rescues the
206 chromosome segregation defects associated with premature loss of sister
207 chromatid cohesion.
208
209 **SAC inactivation suppresses chromosome shuffling after loss of cohesion.**
210 We demonstrated that loss of SAC enhanced mitotic fidelity upon cohesin
211 impairment. The severity of the phenotypes associated with premature cohesion
212 loss is associated with extensive genome randomization. This is enhanced by
213 chromosome shuffling due to engagement of isolated chromatids into error-
214 correction reactions (Khodjakov and Pines, 2010; Mirkovic et al., 2015; Nezi and
215 Musacchio, 2009; Oliveira et al., 2010). We postulated that SAC loss enhanced
216 mitotic fidelity by reducing mitotic timing and thereby limiting the degree of
217 chromosome shuffling. To evaluate this hypothesis, the timing and extent of
218 chromosome shuffling was assessed in cells undergoing mitosis upon premature
219 loss of sister chromatid cohesion in the absence or presence of a functional SAC. In
220 embryos, the SAC-dependent mitotic delay observed upon cohesin cleavage, albeit
221 short (~ 4 min) (Figure 3B), it was nevertheless long enough for a high degree of
222 chromosome shuffling before mitotic exit (movie S7). In the absence of a functional
223 SAC, however, and despite the evident and full premature loss of cohesion, there
224 was a decrease in chromosome shuffling events (Figure 3A and movie S8). Similar
225 results were obtained in wing disc cells, where chromosome-shuffling events after
226 cohesin cleavage were infrequent upon SAC inactivation (Movies S4 and S5).
227

228 Altogether, these results suggest that despite cohesin loss, engaging into error-
229 correction does not take place during early mitotic stages. To test this possibility,
230 we sought out to measure the kinetics of chromosome shuffling onset upon full
231 loss of sister chromatid cohesion. Analysis of chromosome configuration, both in
232 embryos and wing disc cells, revealed that despite cohesin removal, chromosomes
233 retain a pseudo-metaphase configuration for an extended period of time (Figure
234 2A, t=6min; 2C, t=9min; Figure 3A t=2min; see also movies S2, S3,S7). During this
235 pseudo-metaphase stage, sister centromeres were found fully disjoined,
236 confirming loss of sister chromatid cohesion. However, sister chromatid
237 individualization was only initiated later. Even upon full sister chromatid
238 separation, there was an evident delay in the initiation of chromosome shuffling,
239 implying that sister chromatid separation does not trigger immediate error-
240 correction. To confirm this possibility, the timing of error-correction engagement
241 was analysed using kymographs that plot the positioning of centromeres along the
242 segregation plane over time. The time of centromere separation can be easily
243 detected by the split in centromere signals and the onset of chromosome shuffling
244 by the time centromeres start crossing the middle of the segregation plane (Figure
245 3F arrow and arrow heads, respectively). This analysis revealed that upon cohesin
246 cleavage, chromosome shuffling was only initiated 4.07± 0.96 min after NEBD
247 (1.3±0.4min for NEBD to centromere separation and 2.8±0.8min from separation
248 to initiation of shuffling) (Figure 3G). This analysis reveals a significant delay in the
249 initiation of major error-correction events. A similar, yet extended behaviour, was
250 also observed in larvae wing disc cells. Upon NEBD, chromosomes retained a
251 prolonged pseudo-metaphase configuration despite sister chromatid separation
252 (as judged by centromere distances) and chromosome shuffling was only observed
253 much later (11.4± 2.9min after NEBD, Figure S4). The observed delay in extensive
254 shuffling engagement is similar to the mitotic timing in the absence of a functional
255 SAC (Figures 2B,D and 3B). Thus, SAC counteracts genome shuffling in the absence
256 of cohesin by shortening mitosis duration and thereby preventing extensive error-
257 correction.
258
259
260

261 **SAC inactivation restores cell survival after loss of cohesion.**
262 Our results indicate that the mitotic defects upon loss of cohesion are less
263 detrimental in the absence of SAC. If so, the degree of aneuploidy should follow a
264 similar trend. Larvae wing discs are well known to eliminate cells with an
265 erroneous DNA content by apoptosis (Dekanty et al., 2012; Poulton et al., 2014).
266 Therefore, SAC inactivation should reduce the levels of apoptosis after loss of
267 cohesion. To evaluate the extent of apoptosis upon full cohesion loss, larvae
268 carrying a TEV-sensitive Rad21 were heat-shocked to induce TEV protease
269 expression and wing discs were dissected 24h after heat-shock. Virtually no
270 apoptosis was detected (staining for cleaved caspase 3 (CC3)) within the control
271 wing discs ($Rad21^{TEV}$ in the absence of TEV protease) (Figure 4A,B). In contrast,
272 TEV-mediated cohesin cleavage induced high levels of apoptosis within 24hr,
273 extending to over 15±2% (mean ± SD, n=7) of the entire wing disc area (Figure
274 4A,B). Remarkably, the levels of apoptosis were significantly reduced if cohesin
275 loss was induced in the absence of a functional SAC (3±3%, mean ± SD, n=10)
276 (Figure 4A,B). Similar results were obtained upon depletion of San (*san* RNAi),
277 where apoptosis covered approximately 7±4% (mean ± SD, n=5) of the wing disc
278 pouch area, compared to only approximately 0.9±0.6% (mean ± SD, n=6) of the
279 pouch area after co-depletion of San and Mad2 (Figure 4C,D). These results show
280 that inactivation of SAC in a proliferating tissue significantly increases cell survival
281 upon loss of cohesion.
282
283 ## Discussion
284
285 In agreement with the "safeguard" function for the Spindle Assembly Checkpoint,
286 mitotic errors are often exacerbated by impairment of the SAC. These include
287 defects associated with multiple centrosomes, defective microtubule assembly or
288 kinetochore structure (Daniel et al., 2006; Gogendeau et al., 2015; Lee and Spencer,
289 2004; Poulton et al., 2017; Tarailo et al., 2007). Here we demonstrate that the
290 opposite happens with regard to cohesion defects. Absence of the SAC alleviated
291 mitotic errors and improved mitotic fidelity after cohesion loss. Cells with a
292 functional SAC undergo extensive chromosome shuffling and consequent
293 randomization of the genome, whereas virtually no shuffling could be observed in

294 absence of the SAC. The detrimental nature of SAC in the presence of cohesion
295 defects is likely related to the irreversibility of cohesion loss. Most mitotic defects
296 can be corrected over time (e.g. SAC-mediated mitotic delay enables clustering of
297 multiple centrosomes (Basto et al., 2008)). In sharp contrast, premature cohesin
298 loss is an irreversible error and prolonging mitosis duration further enhances
299 genome randomization.
300
301 The improved mitotic fidelity after cohesion loss in the absence of SAC is likely a
302 consequence of slow kinetics of error-correction engagement coupled with a bias
303 for chromosome orientation towards a correct alignment. Several mechanisms are
304 known to bias chromosome segregation towards the right orientation, including
305 centromere geometry (Tanaka et al., 2000), bias in microtubule growth towards
306 the kinetochores (Carazo-Salas et al., 1999; Wollman et al., 2005) and/or
307 kinetochore-mediated microtubule nucleation (Kitamura et al., 2010; Maiato et al.,
308 2004). Of these, chromosome geometry is believed to facilitate bipolar attachment
309 by facing one kinetochore to the opposite pole upon attachment to a pole. If so,
310 what ensures geometric arrangement during the initial mitotic stages, even in the
311 absence of cohesin? A possible mechanism enabling a transient organization of
312 sister chromatids towards opposing poles is incomplete resolution of sister
313 chromatid intertwines. Yet, residual catenation present in metaphase
314 chromosomes is unable to confer functional cohesion as removal of cohesin is
315 sufficient to induce immediate sister chromatid separation (Oliveira et al., 2010;
316 Uhlmann et al., 2000). Additional mechanisms may thus impair prompt resolution
317 of sister chromatids specifically during early mitosis, in contrast what is observed
318 in metaphase chromosomes. Spindle forces were described to enhance
319 decatenation (Baxter et al., 2011; Charbin et al., 2014; Mariezcurrena and Uhlmann,
320 2017) and thus resolution of several DNA-intertwines may only be achieved upon
321 chromosome capture. Recent findings propose that efficient decatenation requires
322 constant "guiding action" from condensin I (Piskadlo et al., 2017). Maximal levels
323 of this complex are only observed on mitotic chromosomes once in late-
324 metaphase/anaphase (Gerlich et al., 2006; Oliveira et al., 2007), which could also
325 limit full decatenation to the later stages of mitosis. Residual catenation is unable
326 to sustain cohesion and chromosome alignment in a SAC competent cell. Yet, it may

327 be sufficient to allow a transient pseudo-metaphase alignment that biases initial
328 chromosome attachment to the right orientation. This is certainly an error-prone
329 process but nevertheless more accurate when compared to total genome
330 randomization due to extensive chromosome shuffling.
331
332 Why separated single sisters are inefficient at triggering error-correction
333 mechanisms during early mitosis remains to be addressed. This could be related to
334 a partial tension state facilitated by pseudo-metaphase chromosomal configuration,
335 precluding error-correction activation. Additionally, an intrinsic delayed action of
336 error correction machinery may further account for observed late shuffling onset.
337 Indeed, slow kinetics or a lag time of Aurora B-mediated chromosome detachment
338 has been hypothesized in several theoretical studies (Kalantzaki et al., 2015;
339 Tubman et al., 2017; Zhang et al., 2013) but so far little experimental observations
340 support this claim. Such intrinsic delay would solve the "problem of initiation of
341 biorientation" whereby initial interactions (necessarily under low tension) are
342 able to survive such a tension-sensitive mechanism for chromosome detachment
343 (Khodjakov and Pines, 2010; Tubman et al., 2017).
344
345 Interestingly, the interplay between mitotic timing and sister chromatid cohesion
346 has been previously reported in mammalian cells whereby extension of mitosis
347 predisposes to sister chromatid cohesion defects. Cells arrested in mitosis for long
348 periods were shown to display sister chromatid separation (referred as "cohesion
349 fatigue") (Daum et al., 2011). Moreover, defective sister chromatid cohesion was
350 described to be synthetically lethal with impaired APC/C function in Warsaw
351 breakage syndrome (WABS) patient-derived cells as well as several cancer cell
352 lines with cohesion defects (de Lange et al., 2015). Our observations now
353 demonstrate how reduction of mitotic timing is sufficient to rescue segregation
354 defects associated with premature cohesin loss. Importantly, these experiments
355 highlight the detrimental effect of the SAC upon cohesion defects. When sister
356 chromatid cohesion is compromised, and thus mitotic fidelity irreversibly affected,
357 the SAC exacerbates mitotic errors in contrast to its canonical protective function.
358

359 # Methods

360

361 ## *Drosophila* strains and rearing conditions

362 *Drosophila melanogaster* flies were raised at 25ºC or 18ºC for hs-TEV containing
363 crosses in polypropylene vials (51 mm diameter) containing enriched medium
364 (cornmeal, molasses, yeast, soya flour and beetroot syrup). All RNAi lines used in
365 the screen (Table S1) are from the Transgenic RNAi project (TRiP) and are
366 available in the Bloomington Drosophila Stock Center. Other *Drosophila* stocks
367 used in this study are indicated in Table S5. To induce full cohesin cleavage in a
368 temporally controlled manner, by TEV protease cleavage, *Drosophila* strains were
369 used with TEV-cleavable Rad21 ($Rad21^{TEV}$) in a Rad21-null background ($rad21^{ex15}$,
370 $Rad21^{271\text{-}3TEV}$-*myc* or $rad21^{ex15}$, $Rad21^{550\text{-}3TEV}$-*EGFP*) (Oliveira et al., 2014; Pauli et al.,
371 2008), in strains mutant or wild type for the Mad2 gene (Althoff et al., 2012; Buffin
372 et al., 2007). TEV expression was induced by heat-shocking 3rd instar larvae at
373 37ºC for 45 minutes. Larvae were then left to recover at room temperature. For
374 live cell imaging, fly strains also expressed *His2AvD-mRFP1* and *Cid-EGFP* (Schuh et
375 al., 2007) fluorescent markers.

376

377 ## *Drosophila* screen Details

378 In the screen we analysed 2955 RNAi lines that theoretically deplete 2920 proteins,
379 corresponding to approximately 21% of all protein coding genes annotated in
380 Flybase (Flybase versionFB2017_06). To select the lines to test we followed a list
381 of available RNAi downloaded from the TRiP website. In this list, the lines are
382 ordered alphabetically, according to gene name or CG number. However, our
383 results do not strictly follow this list, since we mainly used lines constructed with
384 Vallium20 or Valium22 vectors and some lines did not survive shipping. In the
385 screen, females carrying the nubbin-Gal4, UAS-*san* RNAi were crossed with males
386 of different RNAi lines from TRiP (see diagram in Figure S1). The progeny of these
387 flies were classified into different classes according to the adult wing phenotypes:
388 class 1 - wild type wings; class 2 – flies with wings that present only mild
389 morphological defects; class 3- flies whose wing morphological defects are
390 intermediate (similar *san* RNAi); class 4 – flies whose wings show strong
391 morphological defects; class 5 – flies without wings or vestigial wings (Figure 1C)

392 (Wu and Cohen, 2002). The average adult wing class for each condition was always
393 calculated using more than 50 adult flies (n≥50). If the average class for a given
394 genetic interaction was equal or below 2.6 than the RNAi line tested was classified
395 as suppressor, if the average class was equal or above 3.5 than the RNAi line was
396 classified as enhancer (Figure S1). To exclude RNAi lines whose expression by
397 itself led to wing morphological defects, in otherwise wild type imaginal discs, we
398 crossed all lines carrying RNAis identified in the first cross with nubbin-Gal4 and
399 discarded all RNAi lines that were enhancers and produced significant phenotypes
400 by itself (Figure S1).
401
402 **Live imaging**
403 For imaging of wing discs, larval imaginal wing discs were dissected in Schneider
404 medium with 10% FBS. Dissected discs were placed and oriented in a 200 μl drop
405 of medium at the bottom of a glass-bottom petridish (MakTek). Time lapse imaging
406 analysis was performed on a spinning disc microscope using either a Revolution
407 XD microscope (Andor, UK), equipped with immersion a 60x (water) and 100x
408 (oil) objectives (Nikon, Japan) and a iXon +512 EMCCD camera (Andor, UK), or a
409 Revolution XD microscope (Andor, UK) equipped with immersion a 60x glycerol-
410 immersion 1.30 NA objective (Leica Microsystems, Germany) and a 100x oil-
411 immersion 1.4 NA objective (Leica Microsystems, Germany) and a iXon Ultra 888
412 1024*1024 EMCCD (Andor, UK). Stacks of 20-30 frames 0,5 μm apart were taken
413 every 1 to 3 minutes. For syncytial embryo imaging, embryos were aligned on
414 coverslips and covered with Series 700 halocarbon oil (Sigma-Aldrich). Time-lapse
415 microscopy was performed with an inverted wide-field DeltaVision microscope
416 (Applied Precision Inc., Issaquah, WA) in a temperature-controlled room (18–
417 20°C). One stack of 15 frames (0.8 mm apart) was acquired every 30 sec with a
418 100x 1.4 oil immersion objective (Olympus, Japan) and captured by an EMCCD
419 camera (Roper Cascade 1024, Roper Technologies). Movies were assembled using
420 FIJI software (Schindelin et al., 2012) and selected stills were processed with
421 Photoshop CS6 (Adobe).
422
423 **Microinjections**
424 Microinjections were performed as previously described (Oliveira et al., 2010;
425 Piskadlo et al., 2017). 1-1.5 hr old embryos were collected and processed

426 according to standard protocols, and were injected at the posterior pole. Injections
427 were performed using a Burleigh Thorlabs Micromanipulator, a Femtojet
428 microinjection system (Eppendorf, Germany), and pre-pulled Femtotip I needles
429 (Eppendorf). TEV protease was injected at 5 mg/ml TEV protease in 20 mM Tris-
430 HCl at pH 8.0, 1 mM EDTA, 50 mM NaCl and 2 mM DTT.
431
432 **Immunofluorescence**
433 Third instar wing imaginal disc fixation and staining was performed using
434 standard procedures (Lee and Treisman, 2001). Briefly, third instar larvae wing
435 disc tissue (still attached to the larva body) was fixed on ice for 30 min. The
436 fixative consisted of 4% formaldehyde (Polysciences) in 1X PEM buffer solution.
437 Following were washed by gentle agitation three times for 20 min in PBS-T (1x
438 PBS + 0.1% Triton X-100). Primary antibodies incubation was performed
439 overnight at 4 °C in PBS-T supplemented with 1% BSA and 1% donkey serum. The
440 following day, the tissues were washed again and incubated for 2h at room
441 temperature with the appropriate secondary antibodies diluted in PBS-T solution.
442 Finally, after the wash of the secondary antibodies, wing discs were mounted in
443 Vectashield (Vector Laboratories). Fluorescence images were acquired with a ×40
444 HCX PL APO CS oil immersion objective (numerical aperture: 1.25–0.75) on a Leica
445 SP5 confocal microscope. Rabbit anti-cleaved caspase 3 at 1:300 (Cell Signaling,
446 9661S) and anti-Rabbit Alexa Fluor 488 at 1:1000 (Molecular Probes).
447
448 **Quantifications and statistics**
449 Imaging analysis was performed using FIJI software (Schindelin et al., 2012).
450 Statistical analysis and graphic representations were performed using Prism 7
451 software. Multiple comparisons were performed using one-way ANOVA, using the
452 Bonferroni's multiple comparison test. Graphs depict mean ± standard deviations
453 (SD) or mean ± standard error of the mean (SEM), as indicated. Sample size details
454 are included in the respective figure legends.
455

Acknowledgements

We thank S. Heidmann, C. Lehner, R. Karess and the Bloomington Stock Center for fly strains and antibodies, all the members of the Oliveira and Martinho laboratories for discussions, Ricardo Matos for assistance with graphic design and Bárbara Kellen for technical assistance in the pilot screen. We acknowledge the TRiP at Harvard Medical School (NIH/NIGMS R01-GM084947) for providing several transgenic RNAi fly stocks used in this study. The following authors were supported by Portuguese national funding (Fundação para a Ciência e Tecnologia, FCT), fellowships: Rui D. Silva (SFRH/BPD/87482/2012), Mihailo Mirkovic (SFRH /BD/52438/2013) and Om S. Rathore (PD/BD/52428/2013, within the scope of the ProRegeM PhD program Ref. PD/00117/2012, CRM:0027030). Rui Gonçalo Martinho is supported by funding from the Association for International Cancer Research [AICR 10–0553] and the following FCT grants: PTDC/BEX-BID/0395/2014 and UID/BIM/04773/2013 CBMR 1334. Raquel A Oliveira is supported by the following grants: FCT Investigator grant (IF/00851/2012/CP0185/CT0004), EMBO Installation Grant (IG2778) and European Research Council Starting Grant (ERC-2014-STG-638917).

Authors Contributions

R.D.S.: Conceptualization, Investigation, Writing (review & editing). M.M.: Conceptualization, Investigation, Writing (review & editing). L.G.G.: Investigation. O.S.R.: Investigation. R.G.M: Conceptualization, Writing (original draft + review & editing), Funding acquisition. R.A.O.: Conceptualization, Investigation, Writing (original draft + review & editing), Funding acquisition.

Conflict of Interest Statement

The authors declare that they have no conflict of interest.

489 **References**
490
491 Althoff, F., R.E. Karess, and C.F. Lehner. 2012. Spindle checkpoint-independent
492 inhibition of mitotic chromosome segregation by Drosophila Mps1. *Mol Biol*
493 *Cell*. 23:2275-2291.
494 Basto, R., K. Brunk, T. Vinadogrova, N. Peel, A. Franz, A. Khodjakov, and J.W. Raff.
495 2008. Centrosome amplification can initiate tumorigenesis in flies. *Cell*.
496 133:1032-1042.
497 Baxter, J., N. Sen, V.L. Martinez, M.E. De Carandini, J.B. Schvartzman, J.F. Diffley, and
498 L. Aragon. 2011. Positive supercoiling of mitotic DNA drives decatenation
499 by topoisomerase II in eukaryotes. *Science*. 331:1328-1332.
500 Brand, A.H., and N. Perrimon. 1993. Targeted gene expression as a means of
501 altering cell fates and generating dominant phenotypes. *Development*.
502 118:401-415.
503 Buffin, E., D. Emre, and R.E. Karess. 2007. Flies without a spindle checkpoint.
504 *Nature cell biology*. 9:565-572.
505 Carazo-Salas, R.E., G. Guarguaglini, O.J. Gruss, A. Segref, E. Karsenti, and I.W. Mattaj.
506 1999. Generation of GTP-bound Ran by RCC1 is required for chromatin-
507 induced mitotic spindle formation. *Nature*. 400:178-181.
508 Charbin, A., C. Bouchoux, and F. Uhlmann. 2014. Condensin aids sister chromatid
509 decatenation by topoisomerase II. *Nucleic Acids Res*. 42:340-348.
510 Daniel, J.A., B.E. Keyes, Y.P. Ng, C.O. Freeman, and D.J. Burke. 2006. Diverse
511 functions of spindle assembly checkpoint genes in Saccharomyces
512 cerevisiae. *Genetics*. 172:53-65.
513 Daum, J.R., T.A. Potapova, S. Sivakumar, J.J. Daniel, J.N. Flynn, S. Rankin, and G.J.
514 Gorbsky. 2011. Cohesion fatigue induces chromatid separation in cells
515 delayed at metaphase. *Current biology : CB*. 21:1018-1024.
516 de Lange, J., A. Faramarz, A.B. Oostra, R.X. de Menezes, I.H. van der Meulen, M.A.
517 Rooimans, D.A. Rockx, R.H. Brakenhoff, V.W. van Beusechem, R.W. King, J.P.
518 de Winter, and R.M. Wolthuis. 2015. Defective sister chromatid cohesion is
519 synthetically lethal with impaired APC/C function. *Nature communications*.
520 6:8399.
521 Dekanty, A., L. Barrio, M. Muzzopappa, H. Auer, and M. Milan. 2012. Aneuploidy-
522 induced delaminating cells drive tumorigenesis in Drosophila epithelia.
523 *Proceedings of the National Academy of Sciences of the United States of*
524 *America*. 109:20549-20554.
525 Foley, E.A., and T.M. Kapoor. 2013. Microtubule attachment and spindle assembly
526 checkpoint signalling at the kinetochore. *Nature reviews. Molecular cell*
527 *biology*. 14:25-37.
528 Gerlich, D., T. Hirota, B. Koch, J.M. Peters, and J. Ellenberg. 2006. Condensin I
529 Stabilizes Chromosomes Mechanically through a Dynamic Interaction in
530 Live Cells. *Current biology : CB*. 16:333-344.
531 Gogendeau, D., K. Siudeja, D. Gambarotto, C. Pennetier, A.J. Bardin, and R. Basto.
532 2015. Aneuploidy causes premature differentiation of neural and intestinal
533 stem cells. *Nature communications*. 6:8894.
534 Guacci, V., D. Koshland, and A. Strunnikov. 1997. A direct link between sister
535 chromatid cohesion and chromosome condensation revealed through the
536 analysis of MCD1 in S. cerevisiae. *Cell*. 91:47-57.
537 Haering, C.H., A.M. Farcas, P. Arumugam, J. Metson, and K. Nasmyth. 2008. The
538 cohesin ring concatenates sister DNA molecules. *Nature*. 454:297-301.

539 Hou, F., C.W. Chu, X. Kong, K. Yokomori, and H. Zou. 2007. The acetyltransferase
540 activity of San stabilizes the mitotic cohesin at the centromeres in a
541 shugoshin-independent manner. *The Journal of cell biology*. 177:587-597.
542 Kalantzaki, M., E. Kitamura, T. Zhang, A. Mino, B. Novak, and T.U. Tanaka. 2015.
543 Kinetochore-microtubule error correction is driven by differentially
544 regulated interaction modes. *Nature cell biology*. 17:530.
545 Khodjakov, A., and J. Pines. 2010. Centromere tension: a divisive issue. *Nature cell*
546 *biology*. 12:919-923.
547 Kitamura, E., K. Tanaka, S. Komoto, Y. Kitamura, C. Antony, and T.U. Tanaka. 2010.
548 Kinetochores generate microtubules with distal plus ends: their roles and
549 limited lifetime in mitosis. *Developmental cell*. 18:248-259.
550 Lee, M.S., and F.A. Spencer. 2004. Bipolar orientation of chromosomes in
551 Saccharomyces cerevisiae is monitored by Mad1 and Mad2, but not by
552 Mad3. *Proceedings of the National Academy of Sciences of the United States of*
553 *America*. 101:10655-10660.
554 Liu, X., and M. Winey. 2012. The MPS1 family of protein kinases. *Annu Rev Biochem*.
555 81:561-585.
556 Maiato, H., C.L. Rieder, and A. Khodjakov. 2004. Kinetochore-driven formation of
557 kinetochore fibers contributes to spindle assembly during animal mitosis.
558 *The Journal of cell biology*. 167:831-840.
559 Mariezcurrena, A., and F. Uhlmann. 2017. Observation of DNA intertwining along
560 authentic budding yeast chromosomes. *Genes Dev*.
561 Michaelis, C., R. Ciosk, and K. Nasmyth. 1997. Cohesins: chromosomal proteins that
562 prevent premature separation of sister chromatids. *Cell*. 91:35-45.
563 Mirkovic, M., L.H. Hutter, B. Novak, and R.A. Oliveira. 2015. Premature Sister
564 Chromatid Separation Is Poorly Detected by the Spindle Assembly
565 Checkpoint as a Result of System-Level Feedback. *Cell reports*. 13:470-478.
566 Mirkovic, M., and R.A. Oliveira. 2017. Centromeric Cohesin: Molecular Glue and
567 Much More. *Prog Mol Subcell Biol*. 56:485-513.
568 Musacchio, A., and E.D. Salmon. 2007. The spindle-assembly checkpoint in space
569 and time. *Nature reviews. Molecular cell biology*. 8:379-393.
570 Nezi, L., and A. Musacchio. 2009. Sister chromatid tension and the spindle
571 assembly checkpoint. *Curr Opin Cell Biol*. 21:785-795.
572 Ng, M., F.J. Diaz-Benjumea, J.P. Vincent, J. Wu, and S.M. Cohen. 1996. Specification of
573 the wing by localized expression of wingless protein. *Nature*. 381:316-318.
574 Oliveira, R.A., R.S. Hamilton, A. Pauli, I. Davis, and K. Nasmyth. 2010. Cohesin
575 cleavage and Cdk inhibition trigger formation of daughter nuclei. *Nature cell*
576 *biology*. 12:185-192.
577 Oliveira, R.A., S. Heidmann, and C.E. Sunkel. 2007. Condensin I binds chromatin
578 early in prophase and displays a highly dynamic association with
579 Drosophila mitotic chromosomes. *Chromosoma*. 116:259-274.
580 Oliveira, R.A., S. Kotadia, A. Tavares, M. Mirkovic, K. Bowlin, C.S. Eichinger, K.
581 Nasmyth, and W. Sullivan. 2014. Centromere-independent accumulation of
582 cohesin at ectopic heterochromatin sites induces chromosome stretching
583 during anaphase. *PLoS biology*. 12:e1001962.
584 Pauli, A., F. Althoff, R.A. Oliveira, S. Heidmann, O. Schuldiner, C.F. Lehner, B.J.
585 Dickson, and K. Nasmyth. 2008. Cell-type-specific TEV protease cleavage
586 reveals cohesin functions in Drosophila neurons. *Developmental cell*.
587 14:239-251.

588 Piskadlo, E., A. Tavares, and R.A. Oliveira. 2017. Metaphase chromosome structure
589 is dynamically maintained by condensin I-directed DNA (de)catenation.
590 *Elife*. 6.
591 Poulton, J.S., J.C. Cuningham, and M. Peifer. 2014. Acentrosomal Drosophila
592 epithelial cells exhibit abnormal cell division, leading to cell death and
593 compensatory proliferation. *Developmental cell*. 30:731-745.
594 Poulton, J.S., J.C. Cuningham, and M. Peifer. 2017. Centrosome and spindle
595 assembly checkpoint loss leads to neural apoptosis and reduced brain size.
596 *The Journal of cell biology*. 216:1255-1265.
597 Ribeiro, A.L., R.D. Silva, H. Foyn, M.N. Tiago, O.S. Rathore, T. Arnesen, and R.G.
598 Martinho. 2016. Naa50/San-dependent N-terminal acetylation of Scc1 is
599 potentially important for sister chromatid cohesion. *Sci Rep*. 6:39118.
600 Rong, Z., Z. Ouyang, R.S. Magin, R. Marmorstein, and H. Yu. 2016. Opposing
601 Functions of the N-terminal Acetyltransferases Naa50 and NatA in Sister-
602 chromatid Cohesion. *J Biol Chem*. 291:19079-19091.
603 Schindelin, J., I. Arganda-Carreras, E. Frise, V. Kaynig, M. Longair, T. Pietzsch, S.
604 Preibisch, C. Rueden, S. Saalfeld, B. Schmid, J.Y. Tinevez, D.J. White, V.
605 Hartenstein, K. Eliceiri, P. Tomancak, and A. Cardona. 2012. Fiji: an open-
606 source platform for biological-image analysis. *Nat Methods*. 9:676-682.
607 Schuh, M., C.F. Lehner, and S. Heidmann. 2007. Incorporation of Drosophila
608 CID/CENP-A and CENP-C into Centromeres during Early Embryonic
609 Anaphase. *Current biology : CB*. 17:237-243.
610 Sethi, M.K., F.F. Buettner, A. Ashikov, V.B. Krylov, H. Takeuchi, N.E. Nifantiev, R.S.
611 Haltiwanger, R. Gerardy-Schahn, and H. Bakker. 2012. Molecular cloning of
612 a xylosyltransferase that transfers the second xylose to O-glucosylated
613 epidermal growth factor repeats of notch. *J Biol Chem*. 287:2739-2748.
614 Tanaka, T., J. Fuchs, J. Loidl, and K. Nasmyth. 2000. Cohesin ensures bipolar
615 attachment of microtubules to sister centromeres and resists their
616 precocious separation. *Nature cell biology*. 2:492-499.
617 Tarailo, M., S. Tarailo, and A.M. Rose. 2007. Synthetic lethal interactions identify
618 phenotypic "interologs" of the spindle assembly checkpoint components.
619 *Genetics*. 177:2525-2530.
620 Tubman, E.S., S. Biggins, and D.J. Odde. 2017. Stochastic Modeling Yields a
621 Mechanistic Framework for Spindle Attachment Error Correction in
622 Budding Yeast Mitosis. *Cell Syst*. 4:645-650 e645.
623 Uhlmann, F., F. Lottspeich, and K. Nasmyth. 1999. Sister-chromatid separation at
624 anaphase onset is promoted by cleavage of the cohesin subunit Scc1. *Nature*.
625 400:37-42.
626 Uhlmann, F., D. Wernic, M.A. Poupart, E.V. Koonin, and K. Nasmyth. 2000. Cleavage
627 of cohesin by the CD clan protease separin triggers anaphase in yeast. *Cell*.
628 103:375-386.
629 Williams, B.C., C.M. Garrett-Engele, Z. Li, E.V. Williams, E.D. Rosenman, and M.L.
630 Goldberg. 2003. Two putative acetyltransferases, san and deco, are required
631 for establishing sister chromatid cohesion in Drosophila. *Current biology :*
632 *CB*. 13:2025-2036.
633 Wollman, R., E.N. Cytrynbaum, J.T. Jones, T. Meyer, J.M. Scholey, and A. Mogilner.
634 2005. Efficient chromosome capture requires a bias in the 'search-and-
635 capture' process during mitotic-spindle assembly. *Current biology : CB*.
636 15:828-832.

637 Wu, J., and S.M. Cohen. 2002. Repression of Teashirt marks the initiation of wing
638 development. *Development*. 129:2411-2418.
639 Zhang, T., R.A. Oliveira, B. Schmierer, and B. Novak. 2013. Dynamical scenarios for
640 chromosome bi-orientation. *Biophysical journal*. 104:2595-2606.
641
642

643 **Legends**

644

645 **Figure 1. Inhibition of SAC suppresses *san* RNAi-induced adult wing**
646 **developmental defects.**

647 **A.** Tissue-specific RNAi in the pouch of the larvae wing imaginal using the nubbin-
648 Gal4 driver and the UAS/Gal4 system. **B.** Adult wings of wild type *Drosophila*
649 (Oregon R), *Drosophila* expressing a control RNAi (*mCherry* RNAi) or expressing
650 RNAi for san in the larvae wing imaginal discs. **C.** Adult wing phenotypic classes
651 scored during the screen: class 1 (wild type wings); class 2 (weak wing
652 developmental defects); class 3 (*san* RNAi-like wing phenotype); class 4 (highly
653 abnormal wings); class 5 (absence or vestigial adult wings). Additional examples of
654 the scored phenotypic classes are shown in (Ribeiro et al., 2016). **D.**
655 Representative adult *Drosophila* wing phenotypes co-expressing *san* RNAi with
656 *mCherry* RNAi, *mad2* RNAi or *mps1* RNAi in the larvae wing imaginal discs. **E)**
657 Quantification of *Drosophila* wing phenotypes expressing individual RNAi
658 transgenes for *mCherry*, *mad2* or *mps1* (grey bars) or co-expressing *san* RNAi with
659 *mCherry* RNAi, *mad2* RNAi or *mps1* RNAi (black bars) in the larvae wing imaginal
660 discs. Phenotypic quantification of adult wings is mean ± SD of three independent
661 experiments and is based on the classes described in (C) (***$p < 0.0001$, One-way
662 ANOVA with Bonferroni's multiple comparison test; *n* represents the total number
663 of flies evaluated).

664

665 **Figure 2. Inhibition of SAC in wing imaginal discs alleviates mitotic errors**
666 **caused by premature loss of cohesin.**

667 **A.** Images from movies of the wing disc pouch in the control, *san* RNAi and *san* and
668 *mad2* RNAi strains. Strains contained HisH2Av-RFP (red) and CID-EGFP (green).
669 Times are relative to NEDB. Scale bar is 5 μm. **B.** Quantification of mitotic duration
670 in control, *san* RNAi, or *san* and *mad2* RNAi strains. The duration of mitosis was
671 measured from nuclear envelope breakdown (NEBD) to nuclear envelope
672 formation (NEF) using H2Av-RFP channel. Images were taken every 2 minutes.
673 Each dot represents an individual cell and lines represent mean ± SD (n= 71/5 for
674 control, 77/5 for *san* RNAi and 124/5 for *san+mad2* RNAi, n=number of
675 cells/number of independent discs). **C.** Images from movies of the wing disc from

676 strains surviving solely on TEV-cleavable Rad21 (Rad21^{TEV}) with and without
677 heat-shock induced TEV protease cleavage, in strains wild type or homozygous
678 mutant for the *mad2* gene. Strains also expressed HisH2Av-RFP (red) for
679 visualization of mitotic duration and phenotype. Times are relative to NEDB. Scale
680 bar is 5 μm **D.** Quantification of mitotic duration of the no heat shock control, upon
681 TEV-protease mediated cleavage of Rad21^{TEV} and TEV-protease mediated cleavage
682 of Rad21^{TEV} in a *mad2* mutant background. The duration of mitosis was measured
683 from nuclear envelope breakdown (NEBD) to nuclear envelope formation (NEF)
684 using H2AvD-mRFP1. Images were taken every 2/3 minutes. Each dot represents
685 an individual cell and lines represent mean ± SD (n= 27/4 for Rad21^{TEV} - TEV (no
686 HS), 46/8 for Rad21^{TEV} + TEV, 46/4 for Rad21^{TEV}+TEV in a *mad2^{P}* background and
687 60/4 for *mad2^{P}* after heat-shock (HS), n=number of cells/number of independent
688 discs). **E)** Representative images of mitotic cells from *san* RNAi undergoing mitosis
689 with normal and defective chromosome distribution. Scale bar is 5 μm and applies
690 to all images. **F)** Quantification of mitotic exit defects observed in the different
691 experimental conditions; graph represents mean ± SEM of errors of individual
692 discs (n≥4 independent discs corresponding to over 80 cells analyzed per
693 experimental condition).
694
695
696 **Figure 3. Inhibition of SAC in syncytial blastoderm embryos alleviates mitotic**
697 **errors caused by premature loss of cohesin.**
698 **A.** Embryos surviving solely on Rad21^{TEV} either non-injected (up) or injected with
699 5 mg/ml TEV protease (middle and bottom panels). Embryos are derived from
700 females that are wild type or homozygous mutant for *mad2* gene and express
701 HisH2Av-RFP (red) and CID-EGFP (green). Images were taken every 30 seconds
702 and times are relative to NEBD. Scale bar is 10 μm. **B.** Quantification of mitotic
703 duration in un-injected embryos and embryos injected with TEV protease in
704 strains containing solely Rad21^{TEV} and wild type or mutant for *mad2*. The duration
705 of mitosis was measured from nuclear envelope breakdown (NEBD) to nuclear
706 envelope formation (NEF) using HisH2Av-RFP. Images were taken every 30
707 seconds. Each dot represents a single mitosis and lines represent mean ± SD (n=
708 20/4 for Rad21^{TEV} no TEV, 40/8 for Rad21^{TEV} + TEV and 55/11 for Rad21^{TEV}+TEV

709 in a *mad2*^{P} background, n=number of mitosis/number of independent embryos). **C.**
710 Representative image from mitotic exit upon TEV-mediated cohesin cleavage,
711 highlighting how centromere positioning was measured in D; An automatic
712 threshold was used to determine the positioning of centromeres and the area in
713 each pole and between segregating poles was measured. **D.** Quantification of
714 segregation asymmetry in control, cohesin cleavage, and cohesin cleavage in *mad2*
715 mutant background. Each value was quantified by normalizing the area of pole A
716 (with higher area) and the area of pole B (lower area), as illustrated in C; (n= 46/5
717 for Rad21^{TEV} no TEV, 60/6 for Rad21^{TEV}+ TEV and 60/6 for Rad21^{TEV}+TEV in a
718 *mad2*^{P} background, n=number of telophases/number of independent embryos) **E.**
719 Relative area of lagging centromeres in control, RAD21^{TEV} + TEV protease, and
720 RAD21^{TEV} + TEV protease in a *mad2* mutant background; statistical analysis was
721 performed using one-way ANOVA test. **F.** Kymographs of HisH2Av-RFP and CID-
722 EGFP of cells entering mitosis in control, cohesin cleavage, and cohesin cleavage in
723 *mad2* mutant background. Arrow points to centromere separation and arrowhead
724 to the shuffling onset. Scale bars are 5 min and 5 µm. **G.** Quantification of time for
725 chromosome shuffling onset upon TEV-mediated cohesin cleavage, relative to
726 NEBD. Each dot represents a single dividing nuclei from >10 independent embryos.
727
728 **Figure 4. Inhibition of SAC suppresses imaginal wing disc apoptosis caused**
729 **by premature loss of cohesin.**
730 **A.** Images of Cleaved Caspase 3 (CC3) immunofluorescence in controls (Rad21^{TEV}
731 without TEV and *mad2*^{P} after heat-shock (HS)), RAD21^{TEV} + TEV protease and
732 RAD21^{TEV} + TEV protease in *mad2* mutant background after HS. Scale bar is 100
733 µm. **B.** Quantification of CC3 positive area of the entire wing disc, in the indicated
734 experimental conditions; n≥ 5 independent discs per experimental condition;
735 statistical analysis was performed using one-way ANOVA test. **C.** Representative
736 images of CC3 immunofluorescence in control, *san* RNAi and *san* and *mad2* double
737 RNAi. **D.** Quantification of CC3 positive area of the wing disc pouch, in control, *san*,
738 and *san* and *mad2* RNAi; n≥ 4 independent discs per experimental condition;
739 multiple comparison analysis was perform using a one-way ANOVA test.
740

741 **Table 1 - List of genes identified in the screen.**

Type of interaction	CG	Gene [1]	TRiP number	Average wing phenotypic class (*n*)	
				Crossed with Nubbin-Gal4	*Crossed with Nubbin-Gal4 UAS-San RNAi*
Suppressors	CG3100	*Cad99C*	HMS01451	1.00 (240)	2.35 (353)
	CG3399	*capu*	HMS00712	1.00 (161)	2.40 (170)
	CG4625	*Dhap-at*	HMC03654	1.00 (189)	2.49 (211)
	CG3265	*Eb1*	HMS01568	1.00 (175)	2.44 (232)
	CG3161	*His3* [2]	GL00255	2.56 (223)	2.48 (123)
	CG1013	*JMJD7*	HMS00578	1.00 (232)	2.50 (263)
	CG4029	*jumu*	HMS02839	1.00 (186)	2.44 (252)
	CG1749	*mad2*	GLC01381	1.08 (202)	2.04 (224)
	CG7643	*Mps1*	GL00184	1.00 (238)	2.22 (364)
	CG3413	*Nlg4*	HMS01710	1.04 (198)	2.50 (221)
	CG4041	*Parp*	GL00229	1.00 (92)	2.21 (109)
	CG1173	*Sfxn1-3*	HMS01674	1.00 (186)	2.58 (361)
	CG5589	-	HMS00325	2.04 (257)	2.70 (155)
	CG3842	-	HMC02378	1.03 (223)	2.05 (250)
	CG3173	-	HMS02540	1.68 (133)	2.24 (269)
	CG1138	-	HMS02633	1.00 (201)	2.37 (336)
	CG4766	-	HMC02404	1.91 (204)	2.36 (287)
	CG8746	-	HMS02863	1.95 (125)	2.34 (201)
	CG1259	-	GL00498	1.00 (183)	2.48 (382)
Enhancers	CG6875	*asp*	GL00108	1.00 (262)	4.49 (216)
	CG4231	*cno*	HMS00239	1.04 (245)	3.81 (236)
	CG3225	*Claspin*	HMS00772	1.00 (168)	4.27 (182)
	CG8598	*eco* [4]	GL00528	1.00 (191)	4.29 (181)
	GC4203	*Mau2* [4]	HMS02374	1.00 (122)	3.72 (182)
	CG1543	*MFS18*	HMS00961	1.00 (102)	3.98 (164)
	CG2163	*Pabp2*	HMS00553	1.00 (153)	3.91 (206)
	CG3157	*γTub23C*	GL01171	1.05 (229)	3.54 (254)
	CG9773	-	HMS01044	1.11 (192)	4.12 (124)
	CG3224	-	GL00501	1.00 (244)	3.79 (254)

742 [1] The gene abbreviations used are from Flybase version FB2017_06.
743 [2] The RNAi used theoretically also depletes the histone H3 isoforms CG33833, CG33806, CG33839, CG33827,
744 CG33854, CG33824, CG33818, CG33830, CG33863, CG33815, CG33866, CG33836, CG33803, CG33851,
745 CG33809, CG33821, CG33845, CG33857, CG33848, CG33860, CG33842 and CG33812.
746 [3] This RNAi was classified as suppressor due to its strong adult wing phenotype when expressed in the wing
747 imaginal discs with nubbin-Gal4.
748 [4] The genetic interaction with *eco* and *Mau2* has been previously described in (Ribeiro et al., 2016).
749

750 **Table 2** - Main function of the genes identified in the screen.

CG	Gene	Human/Yeast ortologue	Description	Type of interaction	References (PMID)
CG6875	*asp*	ASPM/ -	Mitotic microtubule organization	Enhancer	10073938
CG31009	*Cad99C*	PCDH15/ -	Cell adhesion	Suppressor	11162110
CG42312	*cno*	AFDN/ -	Cell adhesion	Enhancer	22024168
CG3399	*capu*	FMN2/ -	Nucleation of actin microfilaments	Suppressor	17925229
CG32251	*Claspin*	CLSPN/ -	DNA replication checkpoint	Enhancer	22796626
CG4625	*Dhap-at*	GNPAT/ -	Peroxisomal ether lipid synthesis	Suppressor	22758915
CG3265	*Eb1*	MAPRE1/ BIM1	Spindle assembly, dynamics, and positioning	Suppressor	12213835
CG8598	*eco* [1]	ESCO1/ECO1	Cohesion establishment	Enhancer	14653991
CG31613	*His3*	HIST1H3B/ -	Chromatin component	Suppressor	
CG10133	*JMJD7*	JMJD7/ -	Putative histone demethylase	Suppressor	
CG4029	*jumu*	FOXN4/ -	Transcription factor	Suppressor	10940625
CG17498	*mad2*	MAD2L1/ MAD2	Mitotic spindle checkpoint	Suppressor	15075237
CG4203	*Mau2* [1]	MAU2/ -	Cohesion loading	Enhancer	10882066
CG15438	*MFS18*	SLC17A9/ -	Major facilitator superfamily transporter	Enhancer	22359624
CG7643	*Mps1*	TTK/ MPS1	Spindle checkpoint	Suppressor	15556864
CG5589	-	Ddx52/ ROK1	ATP-dependent RNA helicase	Suppressor	28701701
CG3842	-	-/ ENV9	Retinoid-active short-chain dehydrogenase/reductase	Suppressor	19520149
CG31730	-	-/ -	N-terminal acetyltransferase [2]	Suppressor	
CG11388	-	XXYLT1/ -	Protein glycosylation [3]	Suppressor	
CG4766	-	Mab21l2/ -	Cell fate [4]	Suppressor	
CG8746	-	-/ -		Suppressor	
CG9773	-	UNC50/ GMH1	UNC-50 protein family	Enhancer	
CG32243	-	-/ -		Enhancer	
CG12592	-	SLAIN1-2/ -		Suppressor	
CG34139	*Nlg4*	NLGN3/ -	Synaptic adhesion protein	Suppressor	10892652, 24068821
CG2163	*Pabp2*	PABPN1/ SGN1	mRNA polyadenylation	Enhancer	10481015
CG40411	*Parp*	PARP1/ -	DNA repair/transcription	Suppressor	11376691, 24055367
CG11739	*Sfxn1-3*	SFXN1/ FSF1	Mitochondrial ion transmembrane transporter	Suppressor	
CG3157	*γTub23C*	TUBG2/ TUB4	Microtubule organization	Enhancer	1904010

751 [1] The genetic interaction with *eco* and *Mau2* has been previously (Ribeiro et al., 2016).
752 [2] Testis specific paralogue of *Drosophila* Naa20 (CG14222).
753 [3] Homologue to the human xyloside xylosyltransferase 1 that transfers the second xylose to O-glucosylated
754 epidermal growth factor repeats of notch (Sethi et al., 2012)
755 [4] Paralogue of *Drosophila* mab-21 (CG4746).
756

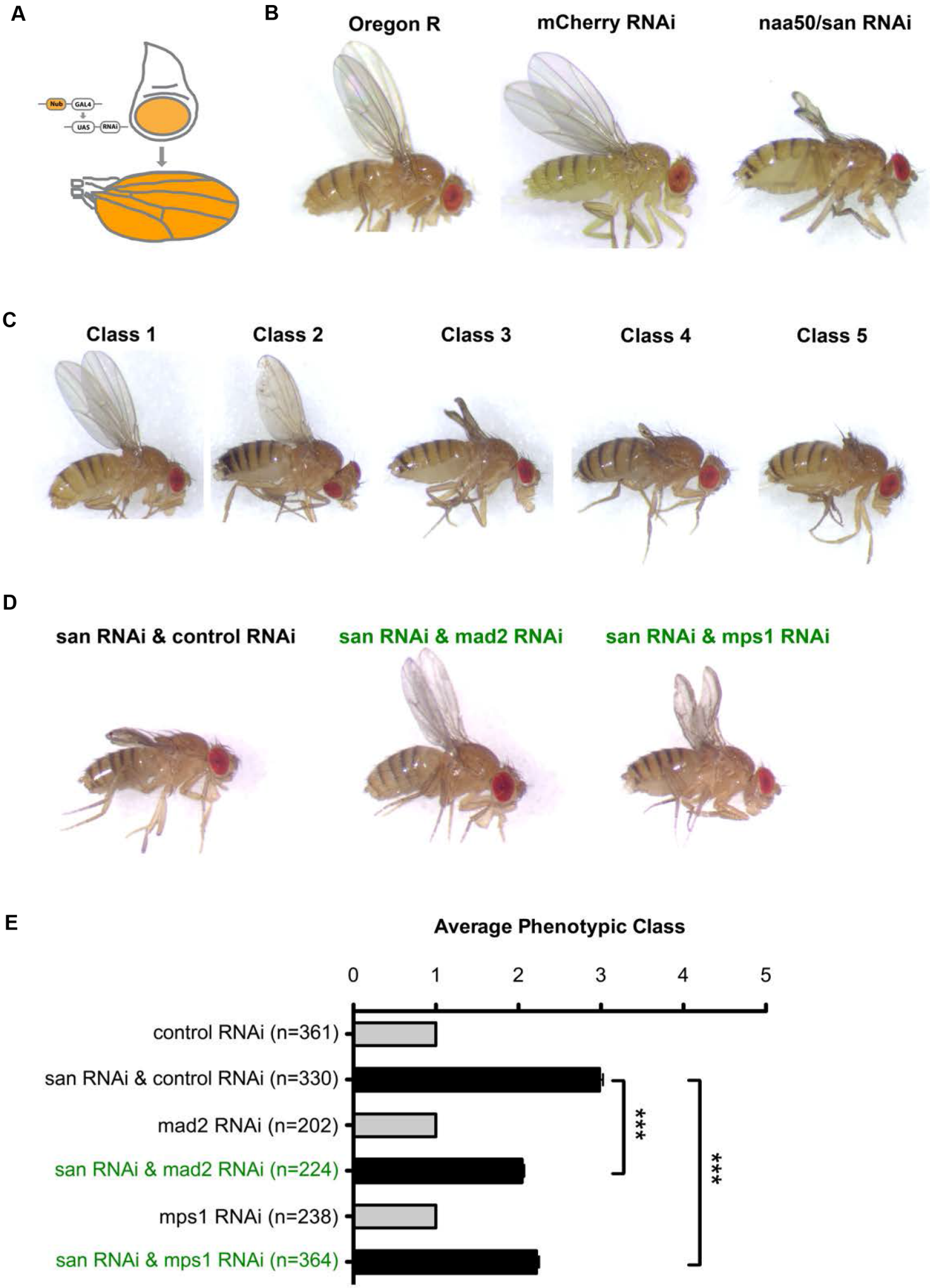

Silva et al - Figure 1

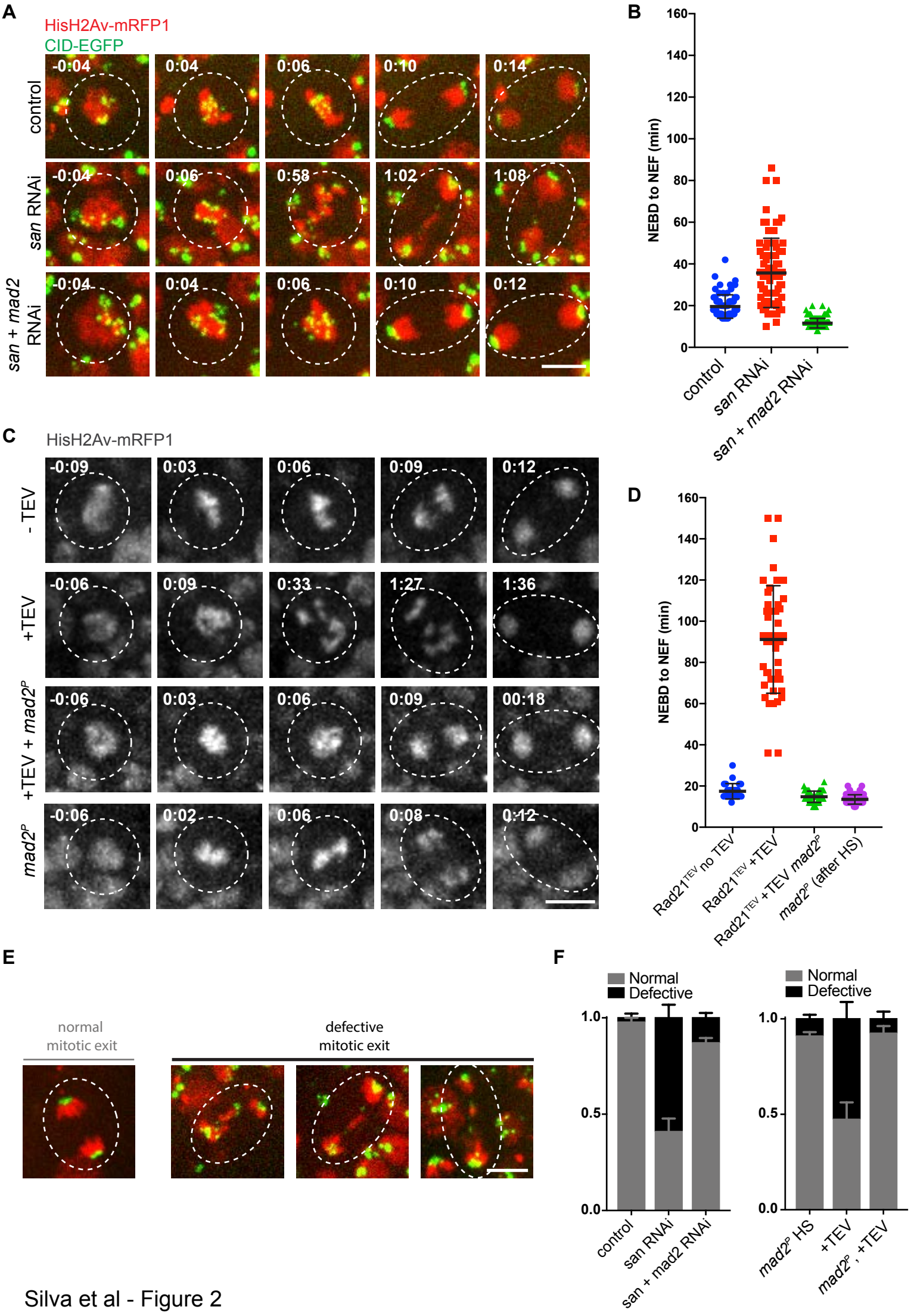

Silva et al - Figure 2

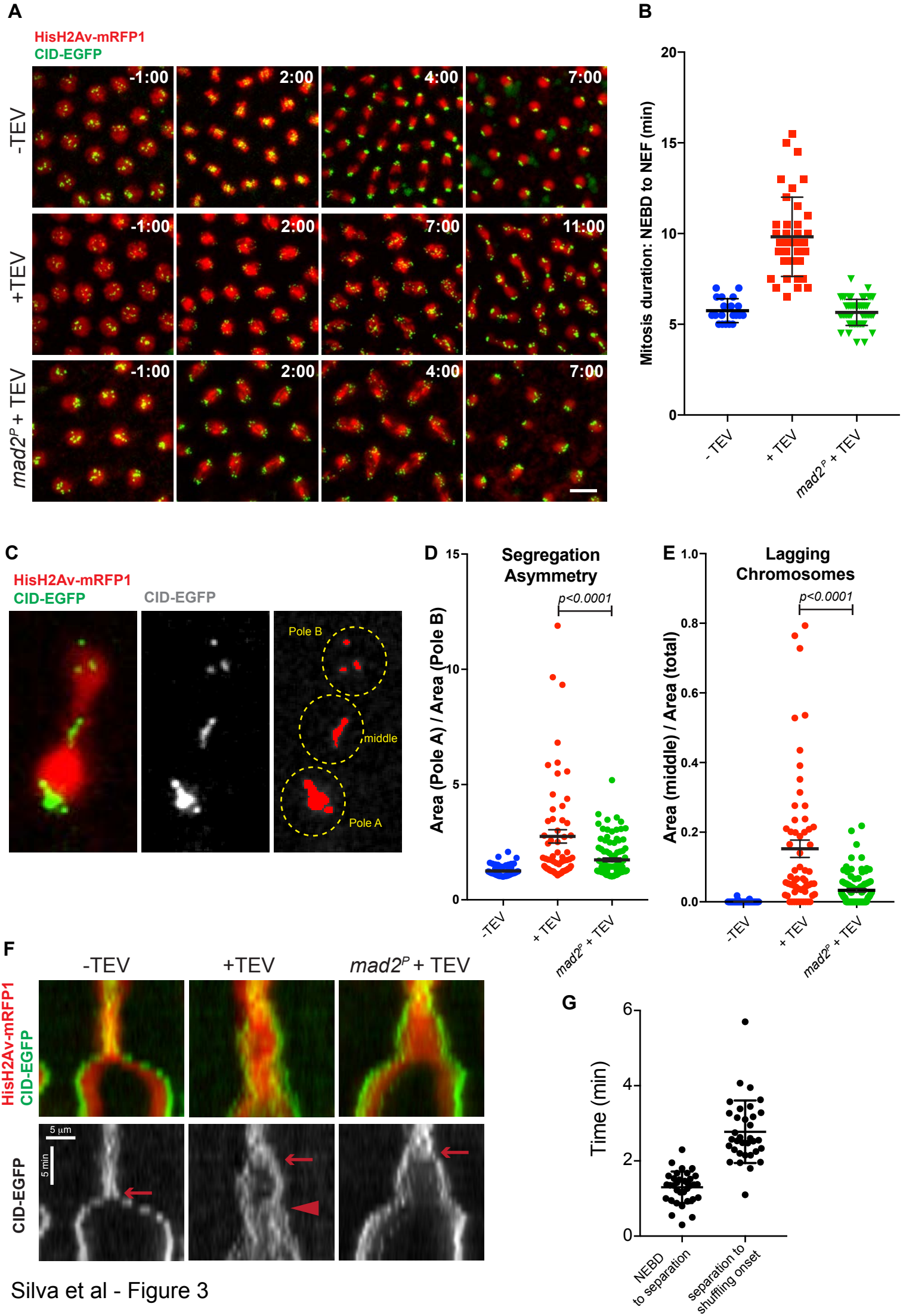

Silva et al - Figure 3

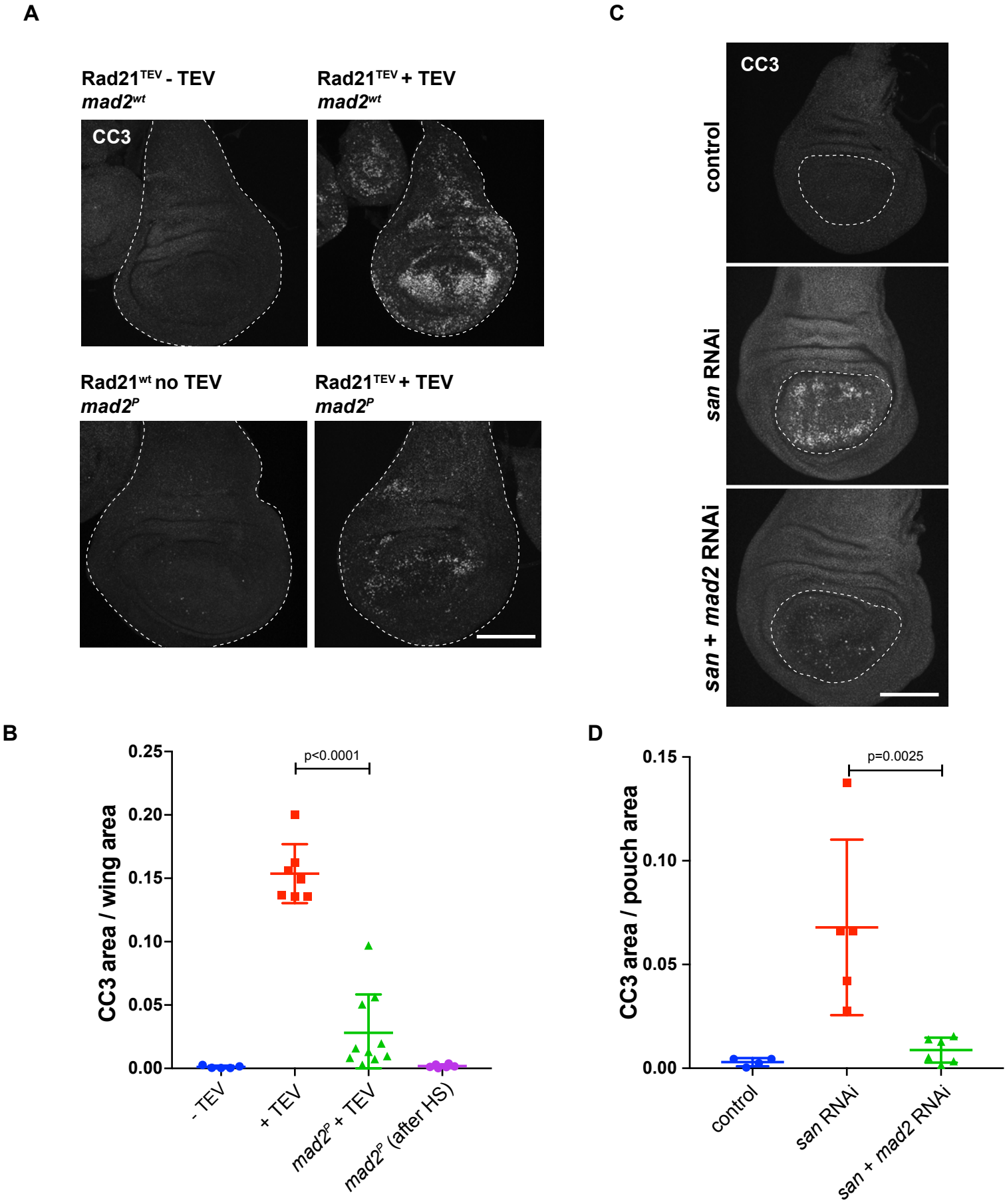

Silva et al - Figure 4